Aero-Optical Simulation in Ansys FLUENT; Application and Validation

Mohammed S. Kamel*
Ansys Inc., 10 Cavendish Court, Lebanon NH 03766, United States

Zoran Dragojlovic†
Ansys Inc., 3240 El Camino Real Suite 290, Irvine CA 92602, United States

Valerio Viti‡
Ansys Inc., 10 Cavendish Court, Lebanon NH 03766, United States

Felipe Mercado§
Ansys Inc., 3001 W Big Beaver Road Suite 404, Troy MI 48084, United States

Rongguang Jia¶
Ansys Inc., 10 Cavendish Court, Lebanon NH 03766, United States

Steven La Cava‖
Ansys Inc., 3001 W Big Beaver Road Suite 404, Troy MI 48084, United States

Physics-based simulation techniques are a powerful tool to gain an understanding of the complex flow features surrounding an optical turret for virtually any flight condition and optical aperture orientation angle. These insights are extremely useful for the the evaluation and enhancement of existing and future airborne laser system's performance. In particular for laser systems, the wave-front phase aberration of the electromagnetic waves plays an important role in the overall performance of the laser beam, this is specifically important with laser communication and targeting. These phase distortions are caused by the interaction of the laser beam with the compressible and turbulent flow-field in the vicinity of the optical aperture and are generally defined as Aero-optical effects. In order to predict the aero-optical effects, it is necessary to resolve a wide range of spatial and temporal flow scales. Therefore, conducting sequential flow and optical simulations becomes challenging in terms of storage and input/output overheads. In the present work, we present and validate a coupled fluid and optical workflow that can simulate with high level of fidelity the aero-optical effects using CFD and numerical optical simulations. In this workflow, the instantaneous 3-D flow-field is interpolated during the CFD simulation onto the optical beam grid to conduct ray-tracing calculations. This workflow utilizes the multi-domain architecture provided by Ansys Fluent. It adopts a one-way coupling of concurrent flow and optical calculations to quantify the instantaneous phase distortion based on the sampled density field. Aero-optical analysis can be expanded for multiple beams in a single flow simulation without compromising performance and load balancing. This paper presents the verification and validation processes conducted for the aero-optical flow of two representative test cases: (I) Under-wing pod and (II) Cylindrical turret with flat window.

*Senior R&D Engineer, Fluid Business Unit; Senior Member AIAA; mohammed.kamel@ansys.com (corresponding author)
†Lead Application Engineer, Regional Pre-Sales Support.
‡Manager Application Engineering, Regional Pre-Sales Support; Senior Member AIAA.
§Lead Application Engineer, Regional Pre-Sales Support.
¶Senior Principal R&D Engineer, Fluid Business Unit.
‖Lead Application Engineer, Regional Pre-Sales Support.

I. Introduction

Turrets with hemisphere-over-cylinder design are widely used in airborne laser systems for a wide range of applications including secured communications, remote sensing and imaging, and high-energy laser weapon systems.

This design concept can point and steer laser beams to cover a vast space by variable azimuth (β) and elevation (γ) angles of the moving optical aperture as shown in Fig. 1(a). At realistic fight conditions, the non-aerodynamic shape of these turrets will lead to the creation of complicated compressible turbulent flow features around the optical aperture. These include boundary layers, separated shear layers and wakes, as schematically presented by Gordeyev and Jumper [1] in Fig. 1(b). At trasonic flight speeds, those flow structures are interacted by local shock waves over the turret surface, leading to an earlier flow separation and strong unsteady density variations over the aperture [2].

The performance of optical system, in terms of defocus, jitter and effective range, will be dramatically affected by the optical phase distortion due to these compressible turbulent flow. This is critical for air-borne laser systems for the applications of communication and targeting, as lasers are a coherent light source, meaning all of the photon packets emitted are in phase, which plays a role in the size and propagation of the beam. For laser communications phase modulation encodes the message into the beam. If optical distortion occurs such that phase is degraded and the received beam becomes incoherent, it could adversely effect the beam and or the integrity of the carried data.

The time-averaged Strehl ratio ($\overline{\mathrm{SR}}$) is a popular simple metric for optical system performance. It is the ratio of the time-averaged of far-field irradiance ($\overline{I}$) to the diffracted-limited on-axis irradiance (I_0):

$$\overline{\mathrm{St}} = \overline{I}/I_0. \tag{1}$$

For simple spatial distributions of wavefront distortion, Strehl ratio can be expressed in a closed form in terms of the variance of the optical phase distortion (${\sigma_\phi}^2$) [3, 4]. Accurate prediction of the phase aberration is necessary especially for short-wavelength optical systems, as discussed in detail in later section II.

Computational Fluid Dynamics (CFD) demonstrates To have accurate aero-optical predictions. It is required to resolve all optically relevant spatial and temporal flow scales. And, that can be fulfilled by adequately resolved Large-Eddy Simulation (LES) without any additional optical subgrid-scale modeling, as theoretically demonstrated by Mani et al. [5]. And with the significant progress of high-performance computing (HPC) and high-fidelity simulation techniques, LES has become an effective prediction tool for computational aero-optics [6].

The practical aero-optical flow problems generally involve 3-D geometry and high-Reynolds number turbulence features. The best candidate for these simulations is hybrid approaches combining LES with a Reynolds-averaged Navier-Stokes (RANS) method which provide a more feasible solution for the design and evaluation of airborne optical systems. Initially, Detached-Eddy Simulation (DES) and its variants gained popularity in the last two decades [7–10], and they were applied to simulate the aero-optical flow over the hemisphere-on-cylinder turret as in the experiment conducted by Gordeyev et al. [11]. In the last few years, wall-modeled LES is proven to provide transient aero-optical predictions with the closet agreement with experimental measurements at high Reynolds numbers and a wide range of subsonic, transonic and supersonic flight speeds [12–15]

The optical phase distortions are calculated based on sampling the 3-D fields of the turbulent density field at a given frequency, determined by the smallest optically-relevant flow time-scales. If the optical calculations are conducted independently after the CFD realization, massive data are required to be written at the optical sampling frequency. Moreover, considering multiple beam orientations during the same CFD simulation for a turret with a conformal aperture dramatically degrades the I/O performance of the overall CFD simulation. Additionally, it becomes necessary to store prohibitively massive data for post-processing in the design and development life-cycle of airborne laser systems

In this work, we avoid the necessity to handle these massive sets of data by adopting Ansys Fluent's multi-domain architecture to orchestrate a one-way coupling between the CFD domain and the optical beam grid(s). In this co-simulation, ray-tracing calculations are conducted in a fully parallelized, load-balanced fashion, concurrently with the CFD simulation based on the instantaneous density and index-of-refraction fields. For a given optical system geometry and flow condition, a single co-simulation could predict optical distortions at different beam directions and aperture orientations. This is essential for the optical performance evaluation and enhancement through a simulation-based design cycle of airborne-laser systems.

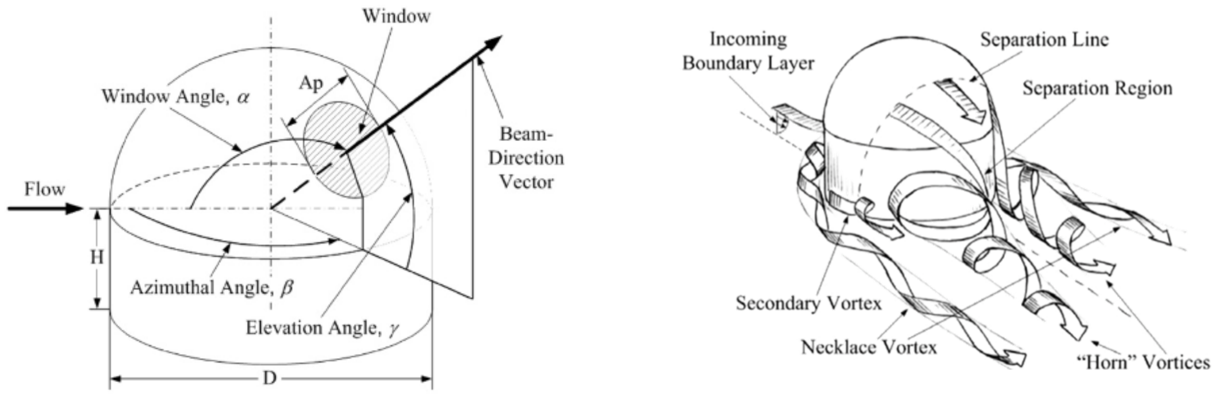

(a) Aperture's elevation angles and azimuthal angles (b) Typical flow structures at subsonic flow speeds

Fig. 1 Hemisphere-over-cylinder design of turrets used in airborne laser systems [1]: (a) maneuverability of optical aperture to point and steer optical beam; (b) Flow-field structures around turret at practical flight conditions

II. Methodology

Multi-domain co-simulation framework in Ansys Fluent is handling the one-way coupling and data exchange from the flow computations in the CFD domain to the ray tracing calculations in the optical grid(s) domain. Fig. 2 shows an example of multiple beam grids constructed for different aperture surfaces. In a single CFD simulation, optical calculations for all multiple beams are conducted simultaneously. The optical grid can be constructed, independently of the aperture surface, with an arbitrary vector of beam propagation as shown in Fig. 3(a) and Fig. 3(b).

In Ansys Fluent, the beam grid is constructed automatically based on geometry parameters, represented by the aperture window, beam length, and vector. As shown in Fig. 3, the beam base represents a planar wavefront attached to the aperture surface. Given a beam length, the beam can be constructed for an arbitrary beam direction and aperture curvature. This is achieved by placing the planar wavefront either at the surface or underneath it. The wavefront resolution will match the given aperture surface mesh, where rays cross face centroids. As illustrated in Fig. 4, the planar wavefront is constructed by projecting the aperture surface along the direction of beam propagation. The ray-tracing calculations are only conducted in the flow region (marked by solid lines); the projected parts (marked by dashed lines) will not be considered in optical computations. By marking the CFD cells along rays, the optical grid-lines match the resolution of the CFD volumetric mesh

The instantaneous density at the optical ray grid points ($\rho_{optical}$) in the grid is interpolated from the density field of bounding cells (ρ_{cv}) in the CFD mesh using a completely partitioned second-order gradient based method:

$$\rho = \rho_{optical} = \rho_{cv} + (\mathbf{x}_{optical} - \mathbf{x}_{cv})\,\nabla\rho|_{cv}. \tag{2}$$

The fluctuating index of refraction n at the ray grid points is calculated using the Gladstone-Dale relation,

$$n = 1 + K_{GD}\rho, \tag{3}$$

where K_{GD} is the Gladstone-Dale coefficient which is weakly dependent on the optical wavelength, but has a nearly constant value of $2.27 \times 10^{-4}\mathrm{m}^3/\mathrm{kg}$. The phase of the wavefront can be described by the instantaneous Optical Path Length (OPL),

$$\mathrm{OPL}(x', z', t) = \int_0^L n(x', y', z', t)dy', \tag{4}$$

where x' and z' are the local coordinates in the aperture plane and y' is the coordinate along the beam path, where L is the beam length. t denotes for time.The phase distortions can be represented by the Optical Path

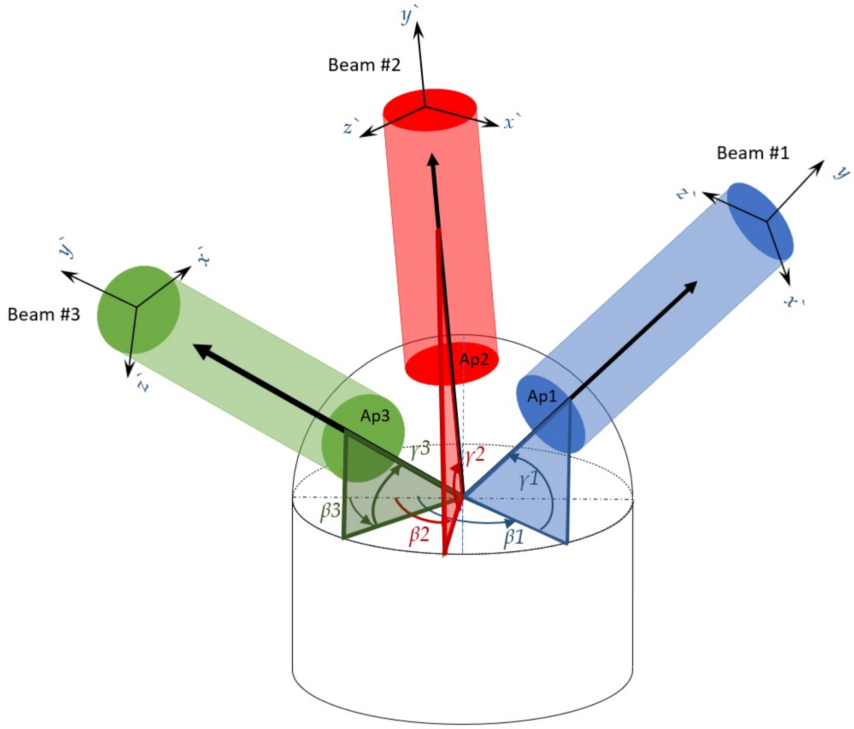

Fig. 2 Constructed multiple beam grids based on apertures surfaces of different azimuthal (β) and elevation (γ) angles

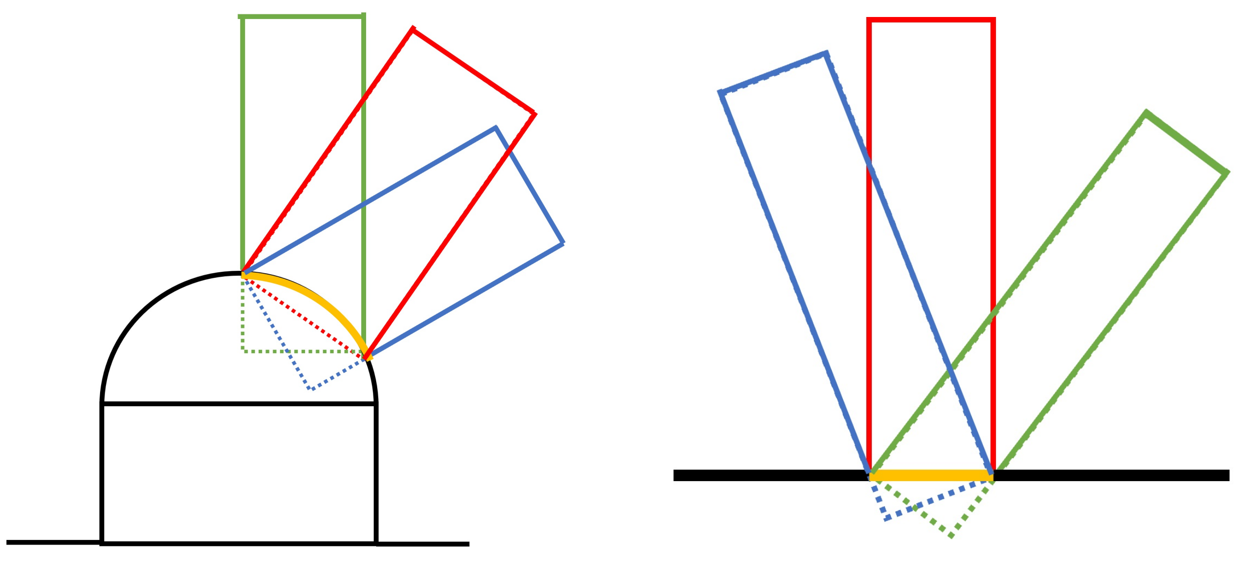

(a)

(b)

Fig. 3 The capability of generating optical beam grid(s) with an arbitrary beam direction for different aperture surfaces. Examples: (a) curved conformal aperture in 3-D turret; (b) flat aperture surface over a flat plate.

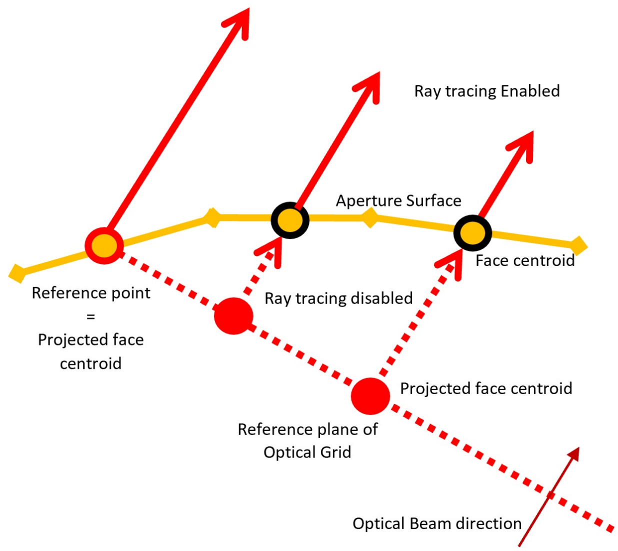

Fig. 4 Construction of optical rays based on the centroids of face elements of the aperture surface.

Difference (OPD). It is calculated based on the relative difference in OPL with respect to its spatial average along the wavefront plane normal to the beam path.

$$\mathrm{OPD}(x',z',t) = \mathrm{OPL}(x',z',t) - \langle \mathrm{OPL}(x',z',t) \rangle, \tag{5}$$

where $\langle \quad \rangle$ indicates the spatial averaging. $\overline{\mathrm{OPD}}$ is the steady lensing term, $\overline{\quad\quad}$ is the time averaging operator. The fluctuating term of OPD (i.e. OPD$'$) is calculated by subtracting the steady lensing term:

$$\mathrm{OPD_{SL}}(x',z') = \overline{\mathrm{OPD}}(x',z'), \tag{6}$$
$$\mathrm{OPD}'(x',z',t) = \mathrm{OPD}(x',z',t) - \mathrm{OPD_{SL}}(x',z'). \tag{7}$$

The low-order terms of OPD (i.e. $\mathrm{OPD_{LO}}$) consists of the zeroth-order and first-order spatially-linear components of OPD$'$:

$$\mathrm{OPD_{LO}}(x',z',t) = \left[C_x(t)x' + C_z(t)z' + C_o(t)\right], \tag{8}$$

where $C_x(t)$ and $C_z(t)$ are the instantaneous slopes of the tilt and tip components in the x' and z' directions, respectively. $C_o(t)$ is the spatial mean of fluctuating OPD, or piston component. These tranisent low-order components are demonstrated in Fig. 5. They are calculated using a least-square method by minimizing the function:

$$G = \iint \left\{\mathrm{OPD}'(x',z',t) - \left[C_x(t)x' + C_z(t)z' + C_o(t)\right]\right\}^2 dx'dz'. \tag{9}$$

The high-order term of OPD (i.e. $\mathrm{OPD_{HO}}$) is calculated by removing the steady lensing, zeroth-order (piston) and first-order spatially-linear (tip/tilt) components from OPD$'$.

$$\mathrm{OPD_{HO}}(x',z',t) = \mathrm{OPD}'(x',z',t) - \mathrm{OPD_{LO}}(x',z',t). \tag{10}$$

The instantaneous and fluctuating terms of OPL and OPD, the steady lensing and both low and high-order terms can be saved and visualized as contour 2-D plots over the aperture surface. For each optical beam, the solver exports time series of the piston, tip/tilt components, the spatially root-mean-square (RMS) of OPD (i.e. OPD_{rms}) and its time-average (i.e. $\overline{\mathrm{OPD}}_{\mathrm{rms}}$), which determine the variance of optical distortion (σ_ϕ^2) as follows:

$$\sigma_\phi = \frac{2\pi\overline{\mathrm{OPD}}_{rms}}{\lambda} \tag{11}$$

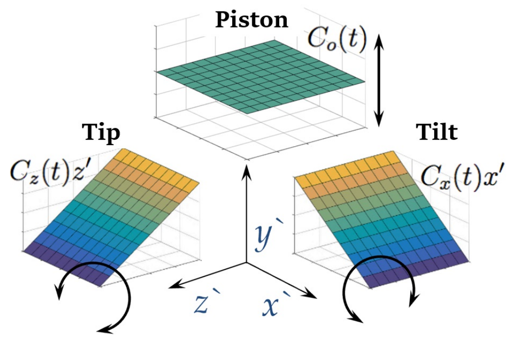

Fig. 5 Illustration of the piston, tip and tilt components of optical distortions of planar wavefront.

As shown in Equation (11), the phase distortion is inversely proportional to the wavelength λ. This makes aero-optical effects more dramatic for short-wavelength optical systems. On the other hand, shorter wavelengths are preferred since the diffraction-limited optical intensity, with a fixed output power and aperture size A_p, scales with ${A_p}^2/(L^2\lambda^2)$, regardless of the aero-optical effects. Therefore, accurate prediction of $\mathrm{OPD_{rms}}$ becomes critical tool in the evaluation and design processes of airborne-laser systems.

III. Verification & Validation

A. Under-Wing Pod with Facing-down Leading Aperture Window

This is first test case presented in the verification process of the concurrent optical calculations. The optical distortions calculated by Ansys Fluent's Aero-Optics feature will be compared to the results of independent verification tool given the same instantaneous density field predicted by the flow solver. It is a generic cylindrical under-wing pod with a 45 deg slanted flat windward face, as shown in Fig. **??**. A CAD model of the pod and supporting structure was created in Ansys SpaceClaim. The shape of the pylon was approximated to match the design of NASA Decoupler Pylon for the F-16 Aircraft [16]. This pod configuration can be used to house a laser device or an EO/IR (Electro-Optical/Infrared) sensor. The pod exhibits a flat optical aperture window facing downwards. The pod dimensions and flow conditions are displayed in Table 1(a) and (b), respectively. The sensor window material is selected to be Sapphire (Al_2O_3) whose material properties is provided by Ansys Mechanical Engineering Materials Database.

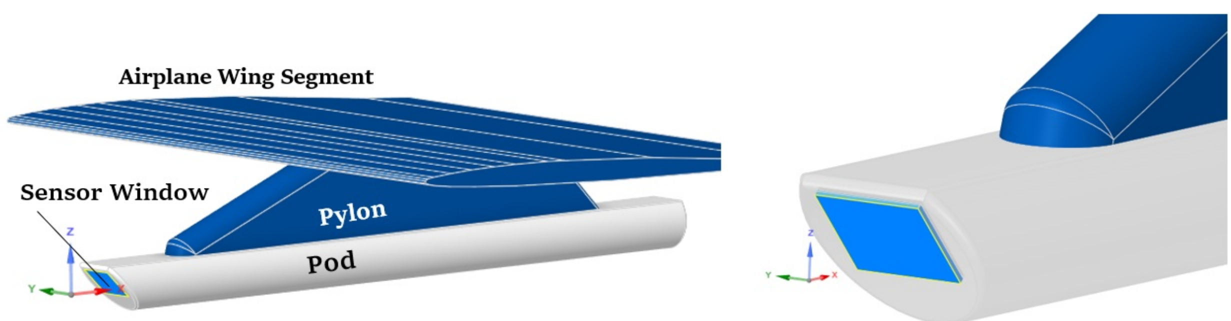

(a) Pod and Supporting Structure

(b) Pod Detail with Sensor Window

Fig. 6 Geometry of Under-wing Pod with Leading Facing-down Flat Window

Pod Dimensions	
Diameter	16"
Length	186.29"
Slant Angle	45°
Window Size	10"×10"
Window Thickness	13 mm

(a)

Flow Conditions	
Flow Speed	$M_\infty = 1.2$
Flow Direction	$-60°$
Side-slip Angle	0°
Altitude	30×10^3 ft
Absolute Pressure	4.373 psi

(b)

Table 1 Under-Wing Pod Dimension and Flight Conditions

The computation domain is a cylinder, as shown in Fig. 7(a).The cylinder diameter is 21.5 m, and its length is 4.572 m. A Poly-hexcore mesh, of 4.6 Million cells, was created for the fluid domain and sensor window using Fluent Meshing as demonstrated in Fig. 7(b)-(e). The fine mesh resolution is concentrated around the pod, with a relatively coarse mesh far away from the pod, where the minimum orthogonal quality equals to 0.08.

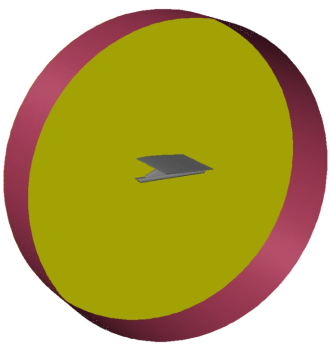

(a) Computational domain

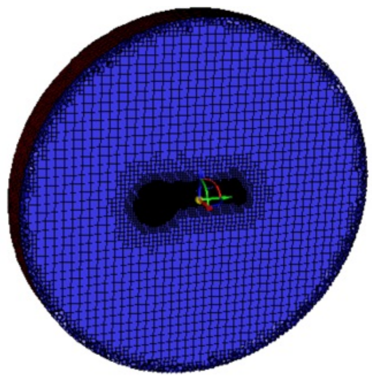

(b) Mesh at a spanwise cut

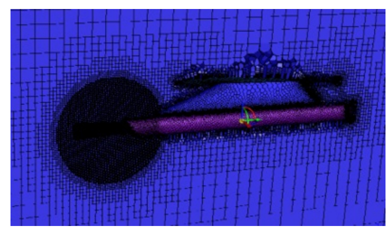

(c) Detailed view near pod

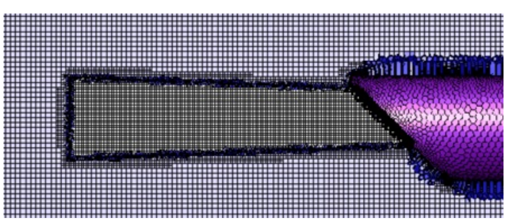

(d) Sampling zone upstream the pod

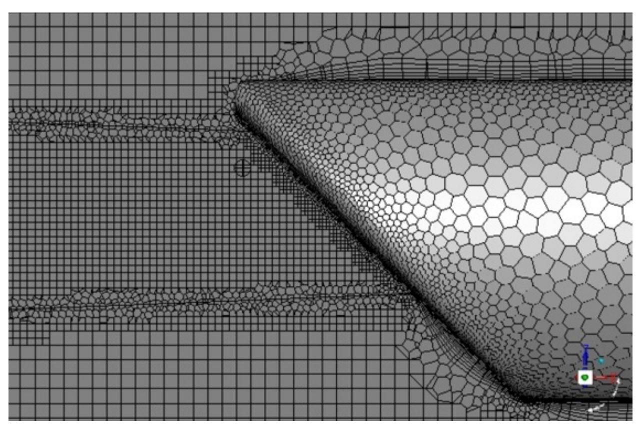

(e) Mesh near the optical window

Fig. 7 Computational Domain and Meshing of Under-wing Pod Case

In this test-case, a pressure-based Unsteady Reynolds-Averaged Navier Stocks (URANS) is employed. Uniform velocity, pressure and temperature conditions are applied far away from the pod and supporting structure. Ideal gas assumption is adopted for air flow with Sutherland's 3-coefficient model for its dynamic viscosity. Turbulence is modeled using Scale-Adaptive Simulation (SAS). No-slip adiabatic boundary conditions are applied on the walls of the pod and its supporting structure. Periodic conditions are assigned at the lateral boundaries in the spanwise direction. Conduction heat transfer is considered through the sensor window. The angle of attack is selected to be $-60°$, such that the flow separates at the sharp leading top edge of the pod and have a separation shear layer upstream the optical window.

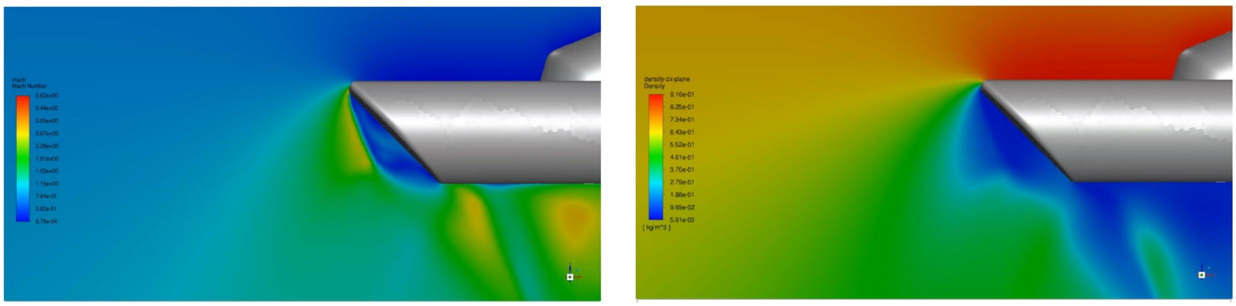

(a) Mach Number

(b) Density

Fig. 8 Geometry of Under-wing Pod with Leading Facing-down Flat Window

For the verification process, we will compare the optical distortions in terms of OPL and OPD calculated by Fluent and compare the results to an analytical tool given the same density field computed by the flow solver. For a single time instant, the 3-D instantaneous density field is collected as shown in Fig. 9 from the sampling zone shown in Fig. 7(d). The optical beam length is 0.9954 m and it is pointed to upstream direction, i.e. the beam vector is $(-1, 0, 0)$.

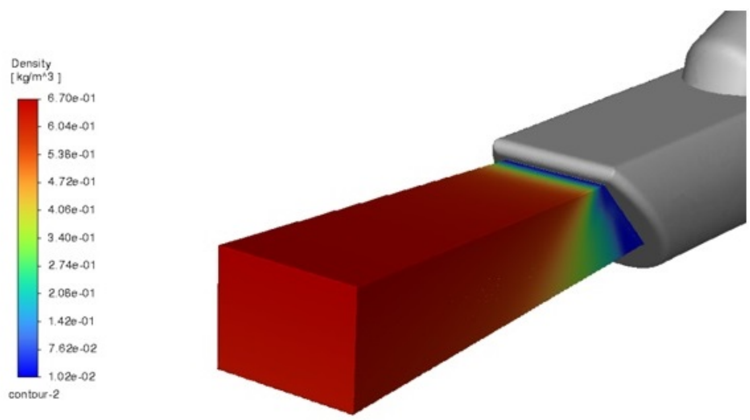

Fig. 9 Density data of a point cloud exported from Fluent

The benchmark analytical tool is a Python-based in-house software, which is based on an algorithm for integrating the density values derived from a point cloud along a specified path, with a particular emphasis on its application in calculating OPL and OPD. The algorithm utilizes the trapezoidal rule for numerical integration and applies linear interpolation using the `LinearNDInterpolator` function from `SciPy v.1.11.4`. This interpolation process is employed to estimate density values at different points along the given path. The density field is initially defined by a point cloud imported from Fluent, as shown in Fig. 9, where each point is associated with a corresponding CFD cell centroid. The integration process is facilitated by subdividing the path into a user-defined integration step, enhancing precision. Following the integration, the accumulated density values are applied to compute the optical path length. The results of OPL and OPD show strong match between Aero-Optics results of Fluent and benchmark resuts, displayed in Fig. 10(a) and (b), respectively. The maximum relative error in OPL and OPD does not exceed 0.7%, as shown in Fig. 10(c).

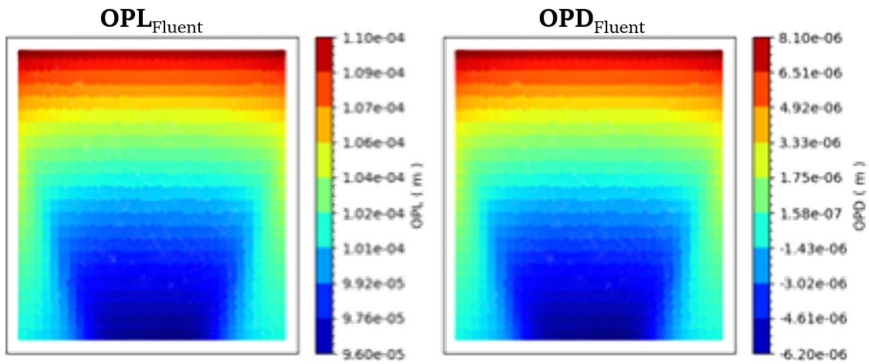

(a) Fluent optical results

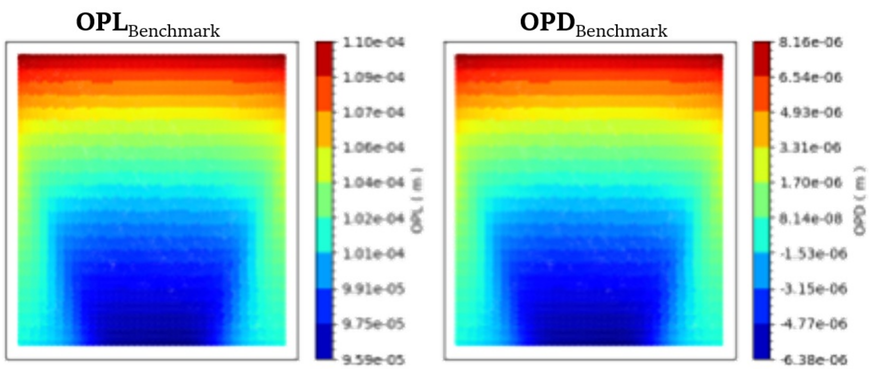

(b) Benchmark optical results

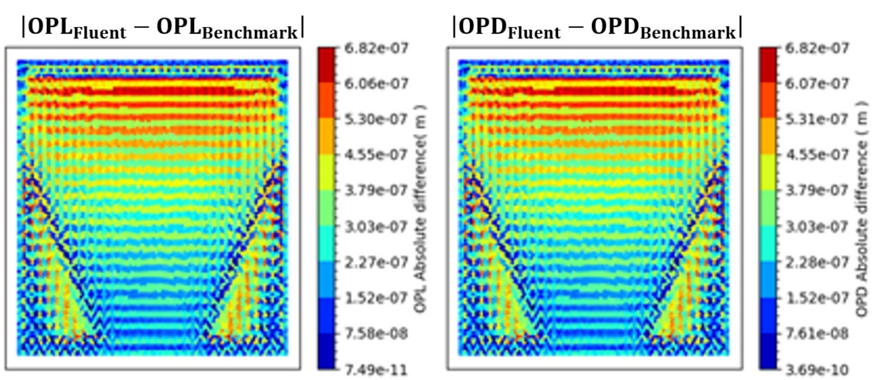

(c) Absolute Error

Fig. 10 Fluent Aero-Optics results of OPL **and** OPD **compared to independent verification post-processing results of the same density field**

This work is currently extended to an ongoing validation progress, where the same set data of the density exported by Fluent transferred to Ansys Zemax OpticStduio. The preliminary results show consistent agreement between the aero-optical predictions by Ansys Fluent and Ansys Zemax.

B. Subsonic Flow Over Cylindrical Turret with Flat Window

The second test case will be used in the validation process of the aero-optical prediction. Gordeyev et al. [17, 18] conducted sets of experiments of subsonic flows over a partial-protruded cylindrical turret mounted between two flat platforms of different altitudes. This configuration, shown in Fig. 11(a), was thoroughly studied as it represents a simplified model of the aero-optical aberrations in the case of 3-D turrets due to the similarities in the separated shear layers over the turrets. The cylindrical turret has a flat window with an elevation angle θ, ranging from 90° to 150°. Flow separation is initiated at its sharp edge, due to Kelvin-Helmholtz instability [19], forming large coherent structures within the region of the laser beam propagation from the aperture.

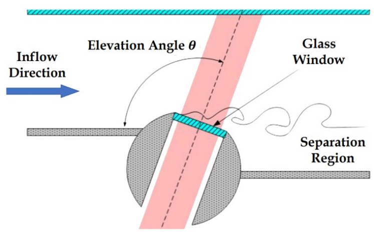

(a) Experimental setup

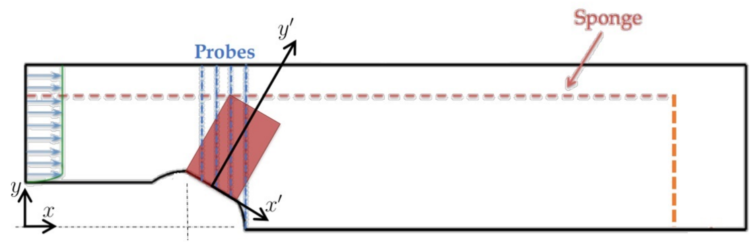

(b) Computational setup

Fig. 11 Schematic of experimental setup [17, 18] and computational domain

The turret dimensions and inflow conditions, represented by the turret radius (R), inlet Mach number (M_{in}), Reynolds number based on momentum thickness (Re_θ) and on the turret radius (Re_R), the window elevation angle (θ), and the inlet boundary layer thickness (δ_{in}) are listed in Table 2(a). A 2-D Shack Hartmann wavefront sensor is used to collect the uncontrolled wavefronts. And the velocity statistics were measured above the aperture at four streamwise stations: $x/R = 3, 3.25, 3.5$ and 3.75, as shown by dashed blues line in Fig 11(b), where x represents the downstream distance measured from the inlet.

Experiment Conditions	
R	2"
M_{in}	0.5
Re_θ	8.5×10^3
Re_R	6.3×10^5
θ	120°
δ_{in}	0.1378 R

(a)

Computational Setup	
L_x	16.8 R
L_y	2.85 R
L_z	0.843 R
L_{beam}	2 R
V_{beam}	$(0.5, 0.8660254, 0)$
L_{sponge}	0.6 R

(b)

Table 2 Flow Conditions and Simulation Setup Parameters

Fig 11(b) demonstrates a schematic of the computational domain. For the turbulent flow computation, unsteady coupled pressure-based Navier-Stokes (PBNS) solver utilizes Large-Eddy Simulation (LES) with WALE Subgrid-scale model (SGS). The Rhie-Chow momentum-based solver uses a Green-Gauss nodal-based second-order schemes for fluxes computations. The air flow adopts the Ideal gas assumption with Sutherland Model for dynamic viscosity. Bounded second-order implicit scheme is used for time marching with Flow Courant Number of 200 and global time step of 5×10^{-6} sec]. Turbulent boundary layer flow is generated at the experimental Reynolds number value in a separate RANS simulation, and fed into the computational domain of the cylindrical turret. Symmetry boundary conditions are applied at the top boundary and the lateral planes along the span. Sponge layer is added at the top and outlet to damp artificial acoustics waves generated boundaries due the limited size of the finite computational domain. The setup parameters, in terms of domain size in streamwise, vertical and spanwise directions (L_x, L_y, L_z), optical beam length (L_{beam}) and vector (V_{beam}) and sponge thickness (L_{sponge}), are listed in Table 2(b).

A mesh sensitivity analysis of the flow and optical prediction by Fluent is examined using CFD mesh of different resolutions. Until this point, the aero-optical simulations are completely conducted using two meshes: Mesh A and Mesh B. Their sizes are 3×10^6 and 25×10^6, respectively. A The meshes are generated by Gmsh [20] by 2-D meshing of a spanwise-cut plan as shown in Fig. 12 using quadrilateral cells with proper distribution and orthogonality in the shear layer region. Then the surface is extruded along the span length (L_z), with 32 and 64 cells, in Mesh A and Mesh B, respectively. A refinement factor of 2 is applied in each direction in Mesh A to generate Mesh B. Fluent results is compared to the corresponding experimental measurements [17, 18] and previous numerical simulation conducted by Kamel et al. [12, 13].

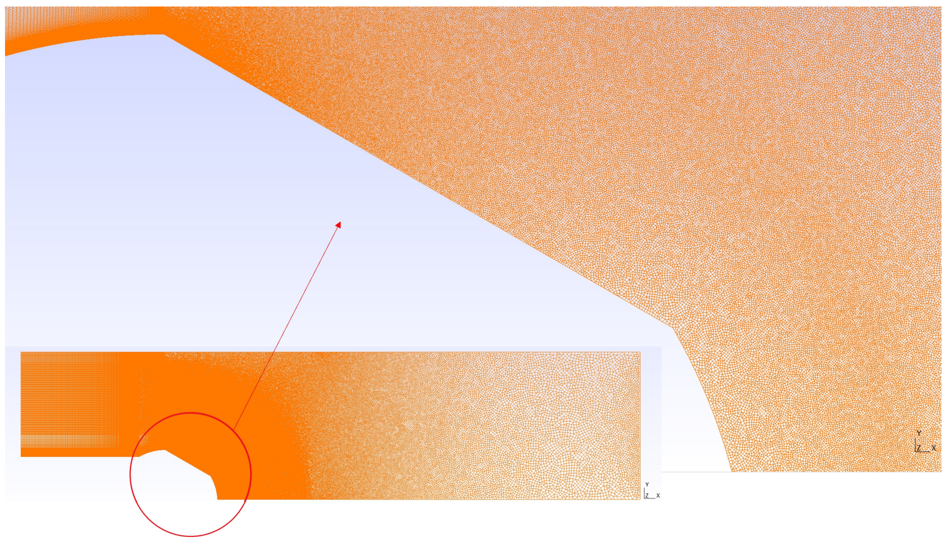

Fig. 12 Detailed view of Mesh B of the cylindrical turret case at the mid-span

The flow visualization of the velocity and density instantaneous fields are shown in Fig. 13 and 14, respectively. A separation bubble is created over the flat aperture, where the flow velocity magnitude and density decreases with respect to the free flow-field. The density jump across the shear layer plays a dominate role in the wavefront distortion, in addition to the effects transient vortical flow structure.

Different components of wavefront distortions can be displayed directly at surfaces representing the optical aperture, as shown in the demonstrated OPL in Fig. 15. In Fig. 16(a-e), the instantaneous OPL, and its derivatives are visualized. The steady lensing term in Fig 16(c), show the effect of the mean density difference across the shear layer above the aperture. The piston and tip/tilt components are composing the optical jitter, whose instantaneous value is displayed in Fig. 16(d) as the low-order terms of OPD $(\text{OPD}_{mathrmLO})$ (see Eq. 8. The high-order terms of OPD_{HO}, displayed in Fig. 16(e), is calculated by removing the steady-lensing term, and instantaneous piston and tip/tilt components, as previously explained in Eq. 10. All the optical calculation are done concurrently with the flow simulation at the same rate of density sampling. The density field is sampled from the CFD mesh every 10 flow time steps, which is equivalent to the least optically relevant flow time scales based on the detailed investigation of the spatial and temporal correlation of OPD discussed in Ref. [12].

After reaching to fully developed turbulent flow-field and statistical convergence, the aero-optical simulations for both meshes A and B start to collect the flow and optical statistics for approximately 7 flow-through-times based on the inlet speed (U_∞) and domain streamwise length (L_x). Time series of piston, tip and tilt are exported from Mesh B as shown in Fig.17(a),(b) and (c), respectively. The instantaneous and time-averaged OPD_{rms} are plotted in 18.

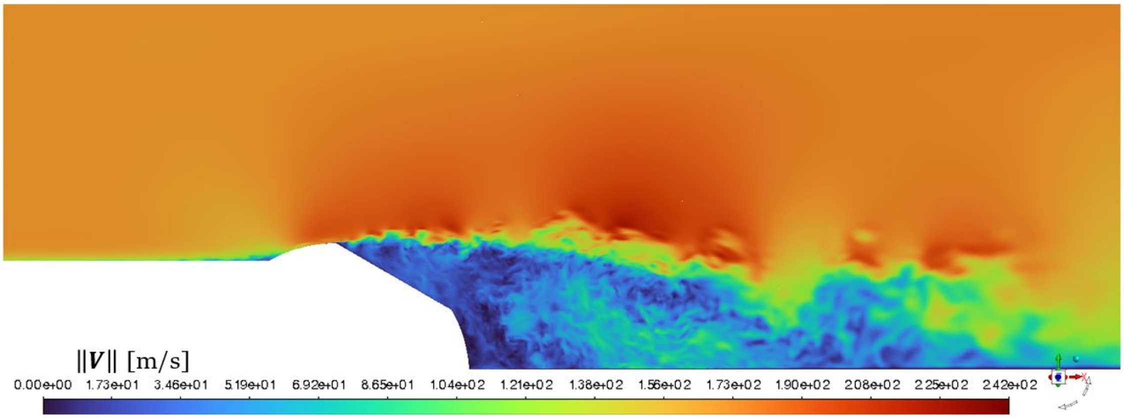

Fig. 13 Visualization of instantaneous velocity magnitude at mid-span of Mesh B

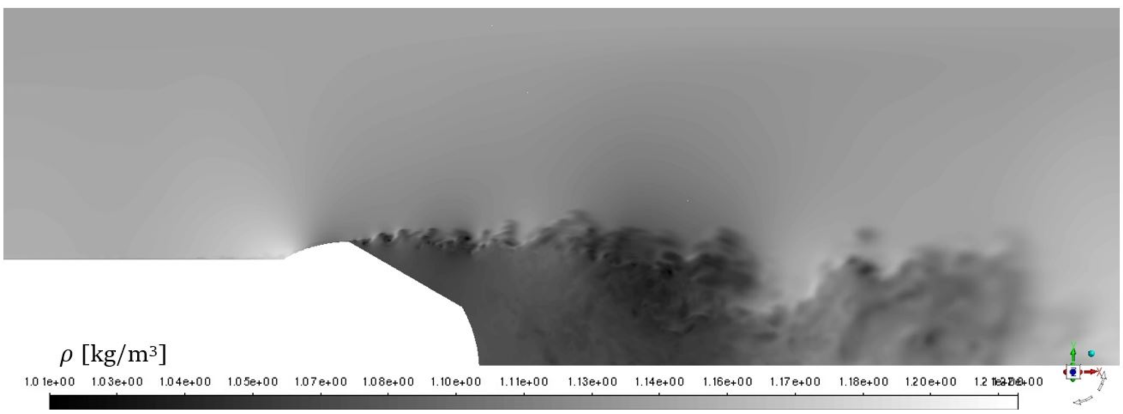

Fig. 14 Visualization of instantaneous density at mid-span of Mesh B

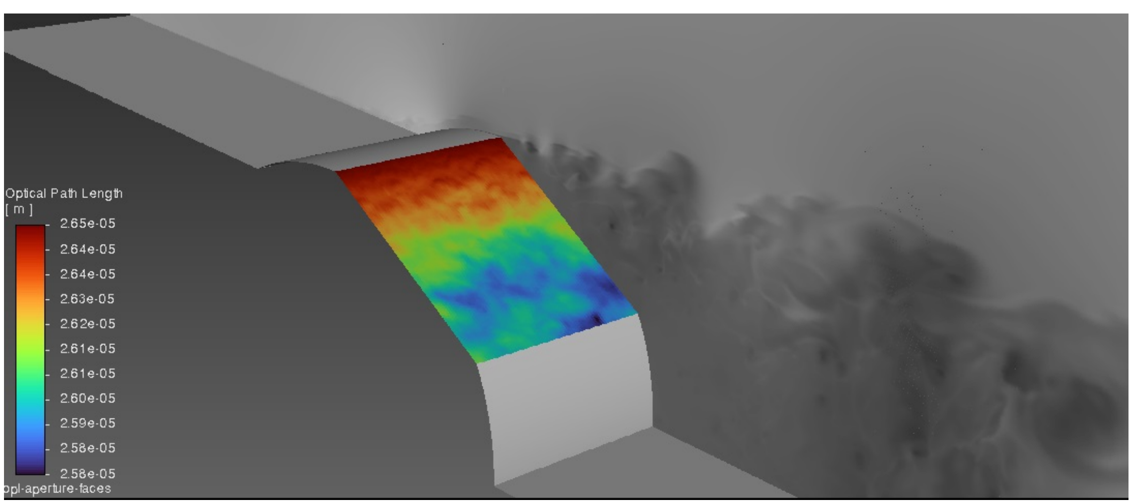

Fig. 15 Visualization of simulated aero-optical flow over the cylindrical turret using Mesh B: Contours of Instantaneous OPL at the aperture and density at the lateral boundary

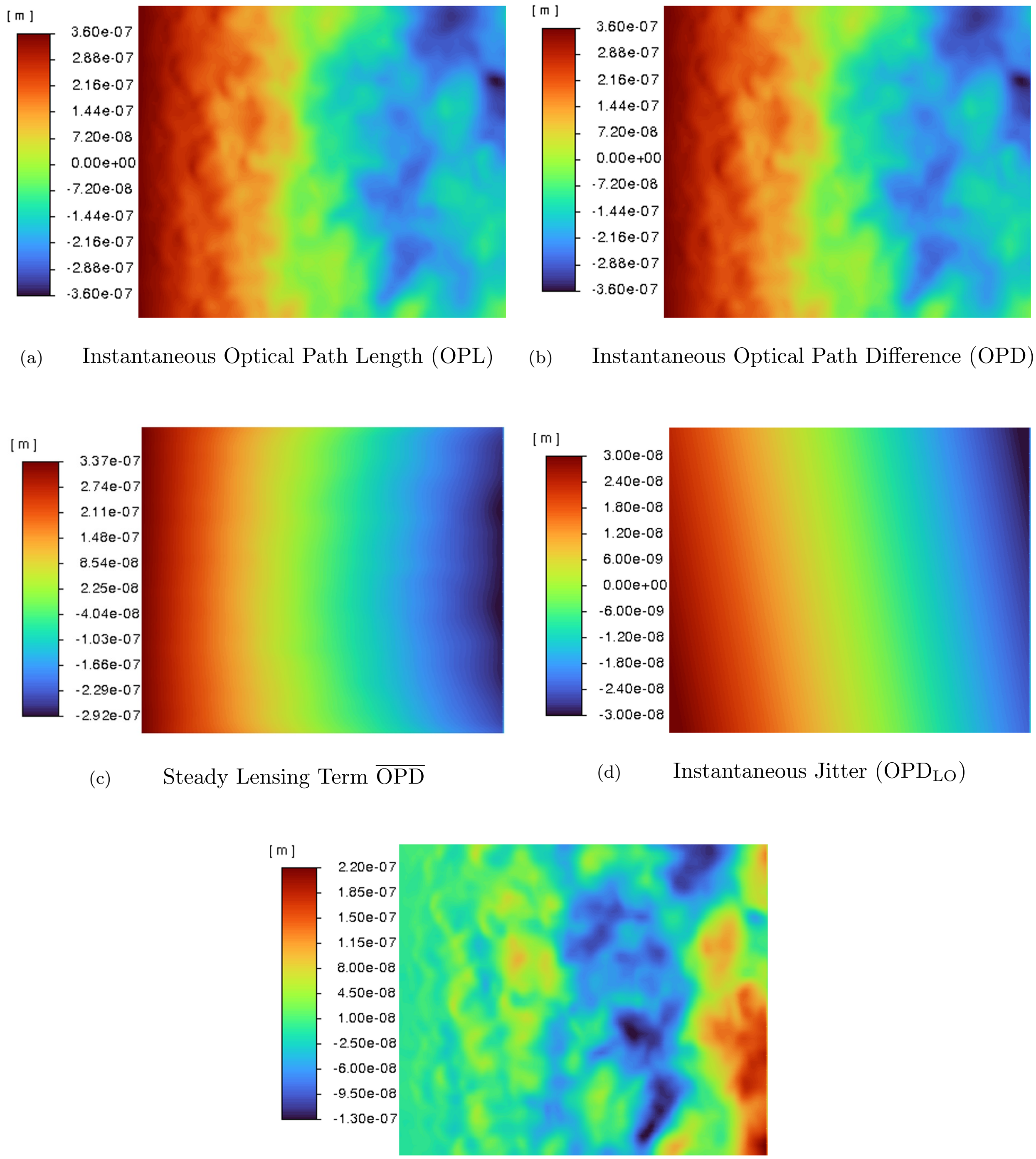

(a) Instantaneous Optical Path Length (OPL) (b) Instantaneous Optical Path Difference (OPD)

(c) Steady Lensing Term $\overline{\text{OPD}}$ (d) Instantaneous Jitter (OPD_{LO})

(e) Instantaneous High-Order Term of OPD (OPD_{HO})

Fig. 16 Visualization of wavefront distortions displayed at the aperture surface of Mesh B

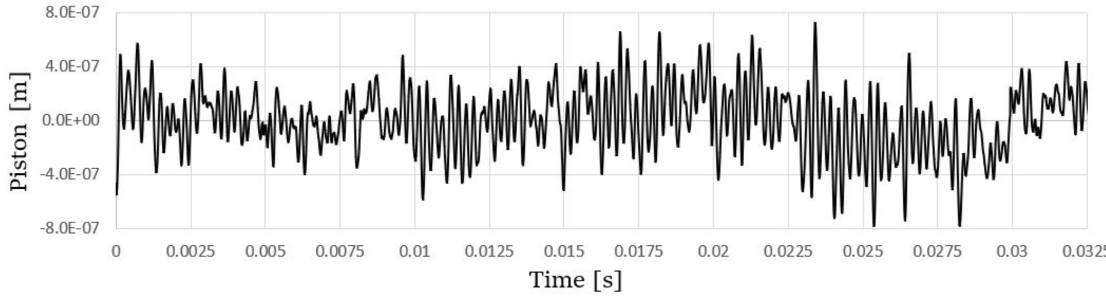

(a)

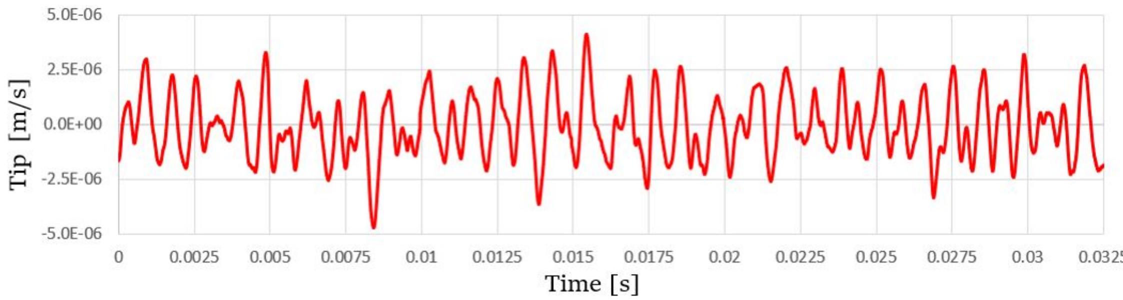

(b)

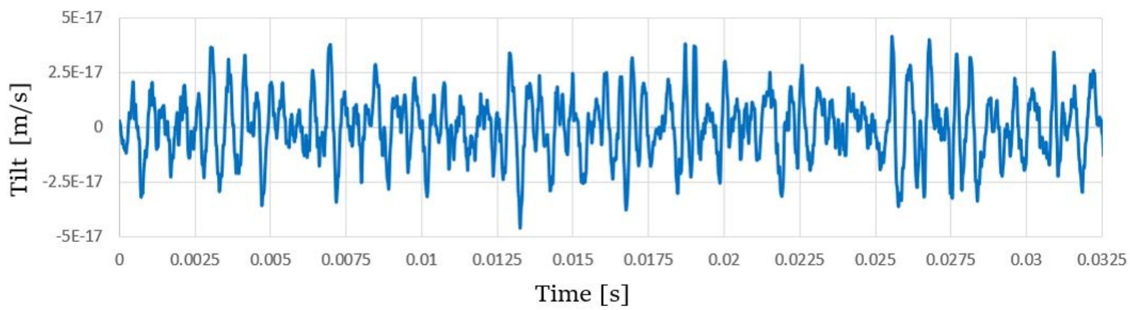

(c)

Fig. 17 Instantaneous components of jitter: (a) Piston $C_o(t)$, (b) Tip $C_x(t)$, (c) Tilt $C_z(t)$.

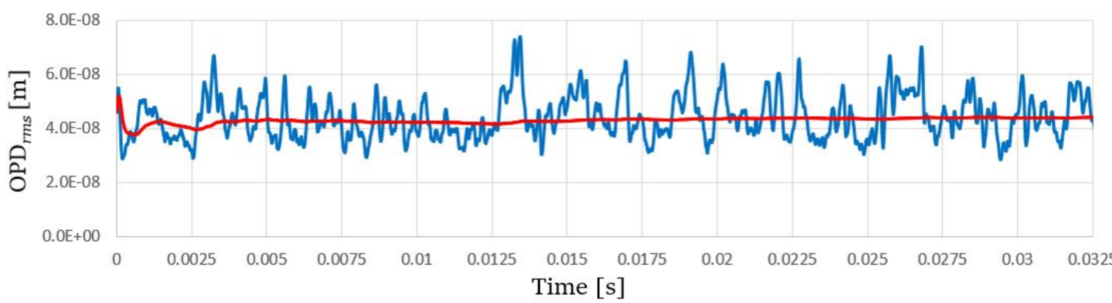

Fig. 18 Spatial RMS of OPD_{rms} after removing the steady-lensing, piston, tip and tilt components: —— (blue), Instantaneous OPD_{rms}; —— (red), time-averaged OPD_{rms} ($\overline{\mathrm{OPD}}_{rms}$).

In Fig. 19 and 20, the Fluent flow solutions of Case A and B of the velocity field at the aforementioned streamwise stations above the aperture, are compared to the experimental measurement [18] and the previous computational results[12, 13] for a relatively fine mesh of 63×10^6 cells. A strong matching of the mean velocity profile between Mesh B and the benchmark data. There is a maximum 10% over-prediction of RMS of velocity fluctuations when comparing the medium mesh B to the fine mesh of Ref. [12].

Fig. 21, 22 and 23 show the temporal RMS of density, temperature and pressure fluctuations, respectively. Prediction of pressure fluctuations shows less mesh-demanding compared to density and temperature. Fig. 23 shows a strong matching in the pressure fluctuations at $x/R = 3.0, 3.25$ and 3.5. In the three figures, there is an overall over-prediction in density, temperature and pressure, with 30% approximately at the center of the separation shear layer, when comparing Mesh B to the previous numerical results using a fine mesh.

Through mesh sensitivity analysis, the mesh refinement of the CFD mesh from Mesh A to Mesh B show correct tendency of the flow prediction to match the previous results of more dense meshes and experimental measurements. Monotonic trend of flow solutions by mesh refinement will be confirmed by the ongoing Fluent simulation of a fine mesh C.

Based on the exported wavefront distortions, as shown in Fig. 18, the non-dimensional values of time-averaged OPD_{rms} from mesh A and B are calculated and listed in Table 3. The relative error compared to the experimental measurements [17, 18] is 30% approximately. This is consistent with the numerical prediction of the density fluctuations in Fig. 21. On the hand, there is an under-estimated $\overline{\text{OPD}}_{rms}$ by the previous numerical simulation [12] using 63×10^6.

Data Source	$\dfrac{\overline{\text{OPD}}_{rms}}{(\rho_\infty/\rho_{SL})DM_\infty^2}$	Mesh Size	Error%
Experimental measurement [18]	1.50×10^{-6}	——	——
Fluent Simulation (Mesh A)	3.86×10^{-6}	3×10^6	157%
Fluent Simulation (Mesh B)	1.98×10^{-6}	25×10^6	32%
Previous Numerical Simulation (Fine Mesh) [12]	1.12×10^{-6}	63×10^6	25%

Table 3 Normalized time-averaged OPD

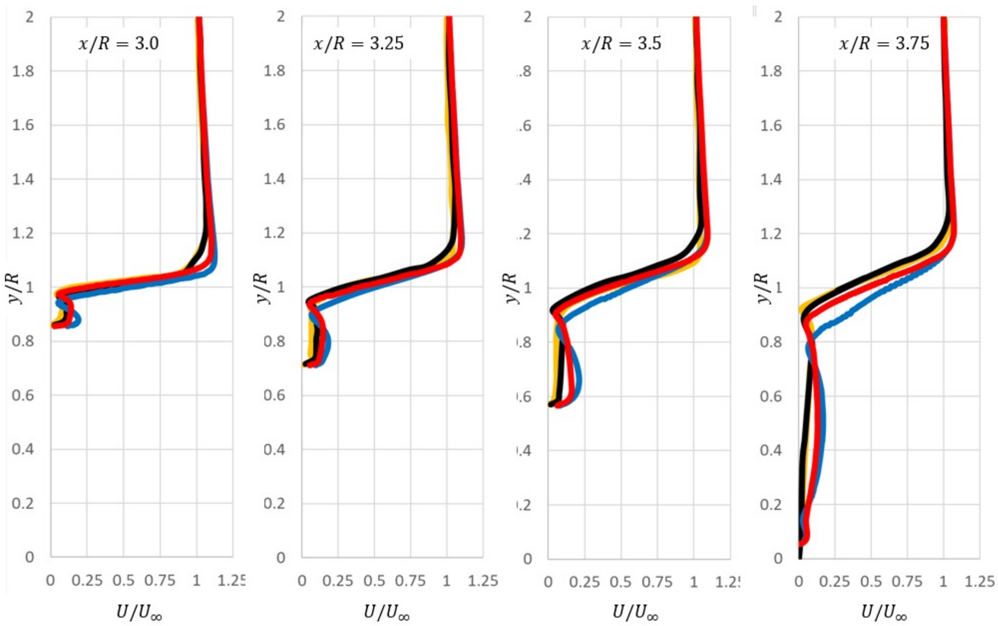

Fig. 19 Mean velocity profiles above the optical window: Fluent results: —— (blue), Mesh A (3×10^6 cells); —— (red), mesh B (25×10^6 cells). —— (black), Kamel et al. [12, 13] (Mesh of 63×10^6 cells). —— (orange), Gordeyev et al. [18].

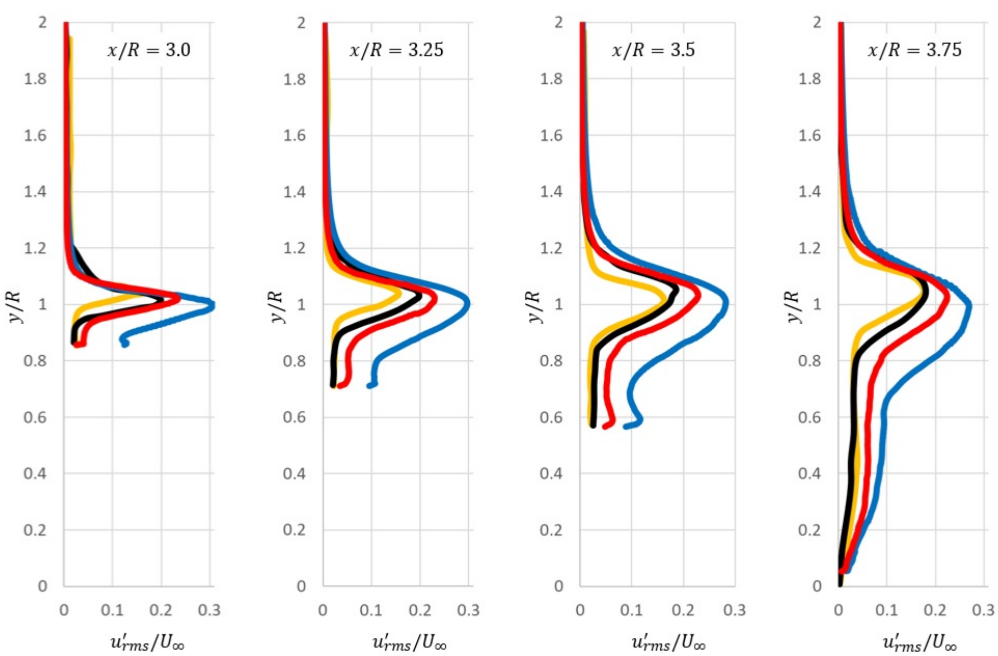

Fig. 20 Root-mean-square of velocity fluctuations above the optical window: Fluent results: —— (blue), Mesh A (3×10^6 cells); —— (red), mesh B (25×10^6 cells). —— (black), Kamel et al. [12, 13] (Mesh of 63×10^6 cells). —— (orange), Gordeyev et al. [18].

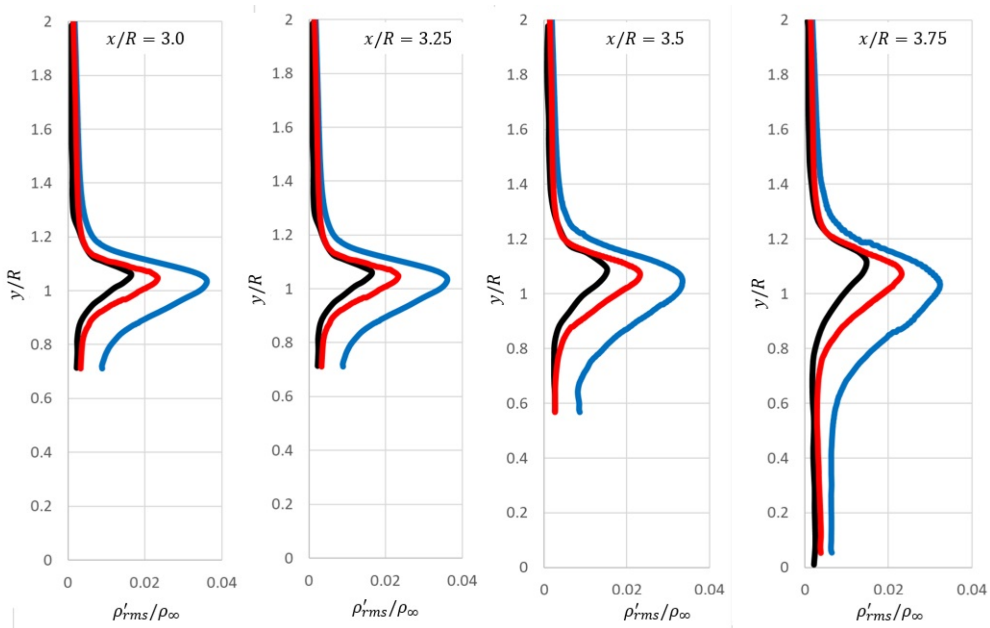

Fig. 21 Root-mean-square of density fluctuations above the optical window: Fluent results: —— (blue), Mesh A (3×10^6 cells); —— (red), mesh B (25×10^6 cells). —— (black), Kamel et al. [12, 13] (Mesh of 63×10^6 cells).

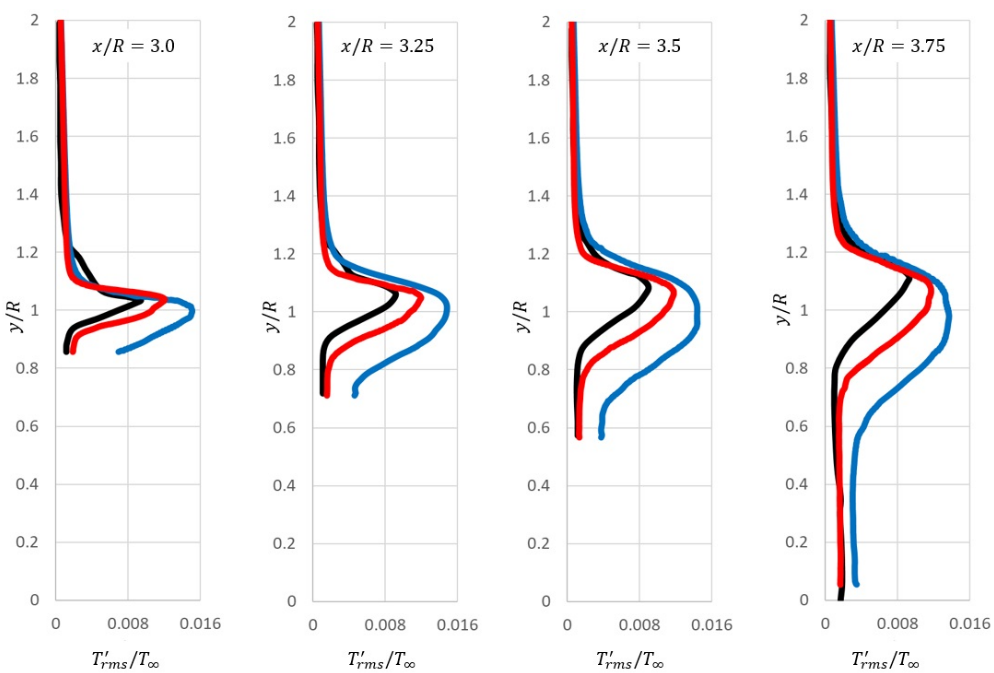

Fig. 22 Root-mean-square of temperature fluctuations above the optical window: Fluent results: —— (blue), Mesh A (3×10^6 cells); —— (red), mesh B (25×10^6 cells). —— (black), Kamel et al. [12, 13] (Mesh of 63×10^6 cells).

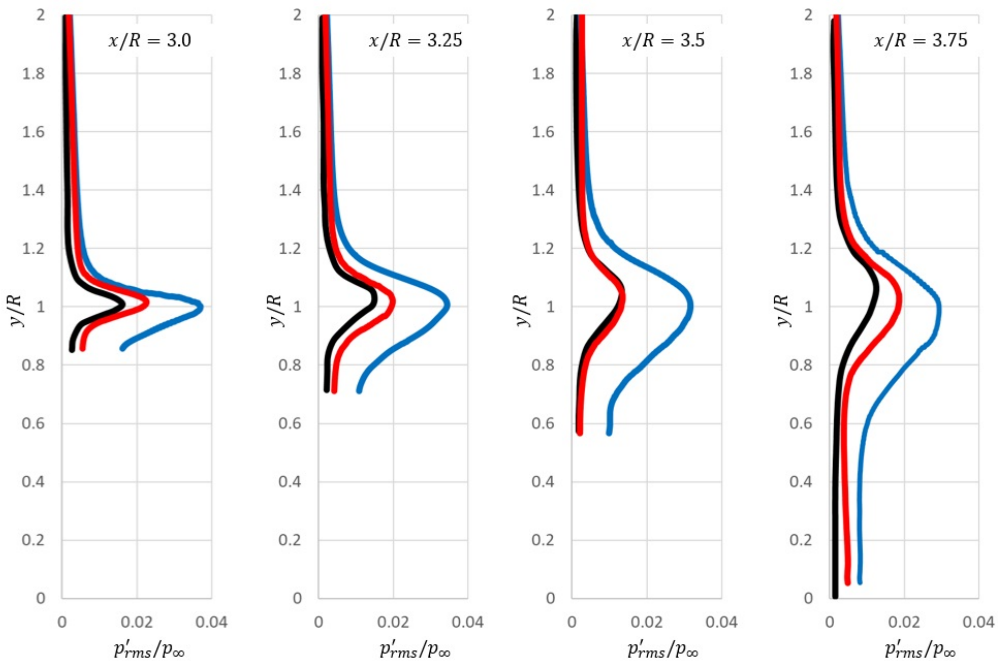

Fig. 23 Root-mean-square of pressure fluctuations above the optical window: Fluent results: ——— (blue), Mesh A (3×10^6 cells); ——— (red), mesh B (25×10^6 cells). ——— (black), Kamel et al. [12, 13] (Mesh of 63×10^6 cells).

IV. Conclusion

This work presented the verification and validation of Ansys Fluent's capability to compute the aero-optical effects on a notional laser beam traveling through a compressible turbulent flow-field. Two test cases were considered. The first case is a verification case of the optical calculations for an under-wing pod in a turbulent, compressible flow at Mach 1.2. The optical results, in terms of OPL and OPD, computed by the CFD solver with Aero-Optics capability were verified against the exact solution computed using an in-house widely validated optical post-processing tool that takes the same density field, computed by Fluent, as an input to the calculation. The second test case under consideration is the aero-optics problem of a cylindrical turret with a turbulent inflow at Mach 0.50. The validation shows positive agreement between the computed flow and aero-optical quantities of interest, $\overline{\mathrm{OPD}}_{rms}$. The proposed aero-optical workflow is embedded in the CFD tool Fluent and makes use of an automatically-generated computational optical mesh overlaid over the original CFD mesh. The computed aero-optical data, OPL, OPD and its components, can be exported to dedicated optical tools such as Ansys OpticStudio for further optical analysis. The concurrent aero-optical CFD calculations will avoid the demand to store massive sets of data to be post-processed, without compromising the simulation performance and scalability.

Acknowledgments

The work presented in this paper is a part of research and development and field testing of the Aero-Optics feature in Ansys Fluent. The authors would like to thank Jeremy McCaslin, Dan Williams, Prasad Alavilli, Joao Mendes Lopes, David Vega and Erin Elliott for the fruitful discussion during the different stages of research and development process of Aero-Optics Feature in Ansys Fluent. Special Thanks to Venkat Ganesh and Rong Ding for their testing efforts.

References

[1] Gordeyev, S., and Jumper, E., "Fluid Dynamics and Aero-Optics of Turrets," *Progress in Aerospace Sciences*, Vol. 46, No. 8, 2010, pp. 388–400.

[2] Jumper, E. J., Gordeyev, S., Cavalieri, D., Rollins, P., Whiteley, M., and Krizo, M., "Airborne Aero-Optics Laboratory-Transonic (AAOL-T)," *AIAA Paper 2015-0675*, 2015.

[3] Mahajan, V. N., "Strehl ratio for primary aberrations in terms of their aberration variance," *JOSA*, Vol. 73, No. 6, 1983, pp. 860–861.

[4] Porter, C., Gordeyev, S., and Jumper, E., "Large-aperture approximation for not-so-large apertures," *Optical Engineering*, Vol. 52, No. 7, 2013, pp. 071417–071417.

[5] Mani, A., Moin, P., and Wang, M., "Computational Study of Optical Distortions by Separated Shear Layers and Turbulent Wakes," *Journal of Fluid Mechanics*, Vol. 625, 2009, pp. 273–298.

[6] Wang, K., and Wang, M., "Aero-Optics of Subsonic Turbulent Boundary Layers," *Journal of Fluid Mechanics*, Vol. 696, 2012, pp. 122–151.

[7] Nahrstedt, D., Hsia, Y., Jumper, E., Gordeyev, S., Ceniceros, J., Weaver, L., DeSandre, L., and McLaughlin, T., "Wind Tunnel Validation of Computational Fluid Dynamics-Based Aero-Optics Model," *Proceedings of the Institution of Mechanical Engineers, Part G: Journal of Aerospace Engineering*, Vol. 223, No. 4, 2009, pp. 393–406.

[8] Ladd, J., Mani, M., and Bower, W., "Validation of Aerodynamic and Optical Computations for the Flow about a Cylindrical/Hemispherical Turret," *AIAA Paper 2009-4118*, 2009.

[9] Morgan, P., and Visbal, M. R., "Numerical Investigation of Flow around a Turret," *AIAA Paper 2007-4480*, 2007.

[10] Morgan, P., and Visbal, M., "Hybrid RANS/LES Simulations for Flow around Two Turret Configurations," *AIAA Paper 2008-0550*, 2008.

[11] Gordeyev, S., Hayden, T., and Jumper, E. J., "Aero-Optical and Flow Measurements over a Flat-Windowed Turret," *AIAA Journal*, Vol. 45, No. 2, 2007, pp. 347–357.

[12] Kamel, M. S., "Aero-Optical Prediction of High-Reynolds Number Flows Using Wall-modeled Large-Eddy Simulation," Ph.D. thesis, University of Notre Dame, 2017.

[13] Kamel, M. S., Wang, K., and Wang, M., "Predictions of Aero-Optical Distortions Using LES with Wall Modeling," *AIAA Paper 2016-1462*, 2016.

[14] Mathews, E. R., Wang, K., Wang, M., and Jumper, E. J., "LES of an Aero-Optical Turret Flow at High Reynolds Number," *AIAA Paper 2016-1461*, 2016.

[15] Kamel, M. S., Wang, K., and Wang, M., "Numerical prediction of aero-optical distortions by transonic flow over a cylindrical turret," *AIAA Paper 2019-0472*, 2019.

[16] Clayton, J., *Design and Fabrication of the NASA Decoupler Pylon for the F-16 Aircraft*, 1985.

[17] Gordeyev, S., Jumper, E. J., Ng, T., and Cain, A., "The optical environment of a cylindrical turret with a flat window and the impact of passive control devices," *AIAA Paper 2005-4657*, 2005.

[18] Gordeyev, S., Cress, J., Smith, A., and Jumper, E. J., "Improvement in Optical Environment over Turrets with Flat Window Using Passive Flow Control," *AIAA Paper 2010-4492*, 2010.

[19] Fitzgerald, E. J., and Jumper, E. J., "The optical distortion mechanism in a nearly incompressible free shear layer," *Journal of Fluid Mechanics*, Vol. 512, 2004, pp. 153–189.

[20] Geuzaine, C., and Remacle, J.-F., "A three-dimensional finite element mesh generator with built-in pre-and post-processing facilities," *Int. J. Numer. Methods Eng*, Vol. 11, 2020, p. 79.